Korean J. Chem. Eng., 40(5), 1122-1132 (2023)
DOI: 10.1007/s11814-022-1278-x

pISSN: 0256-1115
eISSN: 1975-7220

Synergistic degradation of Orange G in water via water surface plasma assisted with β-Bi_2O_3/$CaFe_2O_4$

Weijie Hua and Yong Kang†

School of Chemical Engineering and Technology, Tianjin University, Tianjin 300350, China
(*Received 3 July 2022 • Revised 10 August 2022 • Accepted 30 August 2022*)

Abstract−A coupling method of water surface plasma (WSP) with β-Bi_2O_3/$CaFe_2O_4$ composite was applied to promote the elimination of aqueous Orange G (OG). The morphology, structures, crystal form and chemical bonding state of the prepared β-Bi_2O_3/$CaFe_2O_4$ composite were characterized via SEM, TEM, EDS-mapping, XRD, FT-IR and XPS. The results showed that the addition of composites significantly enhanced the degradation and kinetic constant of OG. The degradation efficiency of the combined system containing 8.0 wt% β-Bi_2O_3/$CaFe_2O_4$ composite was 28.9% higher compared to the sole WSP for OG degradation. The synergistic factor (2.387) demonstrated that the combined system was able to establish a synergistic effect. The effect including peak voltage, air flow rate, initial conductivity and initial concentration of solution on OG removal was inspected. The active species trapping experiments demonstrated ·OH, h^+, $\cdot O_2^-$ and high-energy electrons devoted to OG removal in the combined system. O_3 and H_2O_2 were also involved in the OG removal in the combined system. Three-dimensional fluorescence spectroscopy and liquid chromatography-mass spectrometry were tested to investigate the mechanism of OG degradation. Finally, the combined system in the present study was compared with other competitive technologies for the degradation of OG in the literature.

Keywords: Water Surface Plasma, Orange G, β-Bi_2O_3/$CaFe_2O_4$, Mechanism, Degradation Pathway

INTRODUCTION

Dye wastewater discharged from the textile, printing, paints and cosmetics industries is potentially harmful to the environment and human health [1,2]. More than 700,000 tons of synthetic dyes can be produced each year, of which over 15% are discharged directly as wastewater [3]. Azo dyes are the largest and most versatile class of synthetic dyes, accounting for about 70% of all organic colorants [4]. A number of azo dyes are toxic, mutagenic, carcinogenic and non-biodegradable, which produces an adverse impact on the ecosystem and human health [5]. Orange G is one typical azo dye which is very stable to ultraviolet and visible light radiation. Conventional wastewater treatment technologies typically require long operation time and generate secondary sludge, requiring additional coupled costs [6]. Advanced oxidation processes (AOPs) are effective methods to eliminate refractory and toxic organic compounds via generating strong oxidant ·OH [7]. Among the AOPs, non-thermal plasma (NTP) has played a vital role in wastewater treatment due to its simplicity, economy, high efficiency and environmental friendliness [8].

As one of the NTPs, pulsed high-voltage discharge on the water surface or water surface plasma (WSP) has garnered increasing attention due to its low breakdown voltage, avoidance of corrosion of the discharge electrode, short treatment time and low limitation on the initial conductivity of solution [9,10]. Jiang et al. [11] investigated the water surface gas discharge circulatory airtight reactor system and applied it to degrade methyl orange. Shang et al. [12] compared the yield of H_2O_2 under two gas-liquid mixing forms of gas-phase pulse discharge above the water surface and underwater bubbling pulse discharge. Jose et al. [13] investigated the degradation effect of water surface pulsed corona discharge on the toluene and methyl isobutyl ketone (MIBK) in aqueous solution. In addition to generating O_3 in the gas phase, high-energy electrons will continuously bombard the gas-liquid interface during discharge, which causes the dissociation of H_2O molecules to generate ·OH [14]. More importantly, since the discharge electrodes are located in the gas phase above the liquid surface, WSP is expected to treat organic wastewater with high conductivity, thus accelerating industrial applications. Nevertheless, low energy efficiency is often a problem for NTP. The reason for this is that the considerable physicochemical effects are not fully utilized during discharge.

Due to its narrow band gap (2.1-2.8 eV), non-toxicity and stability, Bi_2O_3 has been used for the degradation of various organic dyes [15]. Bi_2O_3 possesses six polymorphic forms, including α, β, γ, δ, ε and ω phases [16]. With relatively narrow band gap (less than ~2.50 eV), β-Bi_2O_3 has become the favorable material for photocatalysis [17]. Notwithstanding, the photocatalytic activity of β-Bi_2O_3 is restricted due to its relatively low quantum efficiency. To restrain the rapid recombination of electrons and holes, the construction of heterojunctions by coupling with other semiconductors has been proven to be an effective way. $CaFe_2O_4$, which belongs to the ferrite family, is a promising photocatalyst due to its narrow band gap (1.9 eV), low preparation cost and unique catalytic properties [18, 19]. With a suitable band gap and high stability, $CaFe_2O_4$ may be a candidate semiconductor material for constructing an effective heterojunction with β-Bi_2O_3 [20,21]. Furthermore, since the conduc-

†To whom correspondence should be addressed.
E-mail: ykang@tju.edu.cn

tion band value of β-Bi_2O_3 is higher than the reduction potential of O_2 ($E^0(O_2/\cdot O_2^-)$=−0.33 V_{NHE}) [22], O_3 generated during the discharge is adopted as the electron trapping agent [23]. Since ultraviolet light and O_3 can be generated simultaneously in WSP system, the WSP system could establish a synergistic effect with β-Bi_2O_3/$CaFe_2O_4$ photocatalyst [24-26]. The advantages are as follows: first, the β-Bi_2O_3/$CaFe_2O_4$ composites could utilize the ultraviolet light produced via WSP to generate electron-hole pairs. Second, heterojunction could suppress the electron-hole recombination of β-Bi_2O_3. Third, electronegative O_3 existing in WSP and the conduction band electrons of β-Bi_2O_3 can be fully utilized. However, there are hitherto few reports on applications of this distinctive combination of WSP with Bi_2O_3-based composites to treat textile organic wastewater.

Herein, we propose a combining technique of introducing β-Bi_2O_3/$CaFe_2O_4$ composites into the WSP system to synergistically degrade OG dyes in aqueous solution. The morphology and structure, crystal form and chemical bonding state of the prepared samples were first characterized. The removal performance and synergistic effect of WSP system combined with β-Bi_2O_3/$CaFe_2O_4$ composites for OG removal were then investigated. The effect of operational parameters on OG removal was evaluated, as well as the reusability and stability of the catalyst. Moreover, the degradation mechanism was explored in depth by free radical trapping experiments and detection of oxidizing molecules. Three-dimensional fluorescence and liquid chromatography-mass spectrometry (LC-MS) were utilized to analyze the decomposition process of OG molecules. Finally, the combined system was compared with other AOPs used for OG degradation.

EXPERIMENTAL

1. Chemicals

Orange G (OG) was purchased from Macklin (Shanghai, China). Sodium carbonate anhydrous, ethylene glycol and nitric acid were obtained from Tianjin Jiangtian Chemical Technology Co., Ltd, China. Bismuth nitrate pentahydrate and potassium dihydrogen phosphate were procured from Tianjin Kemiou Chemical Reagent Co., Ltd, China. Ferric nitrate nonahydrate, calcium nitrate tetrahydrate and citric acid were acquired from Aladdin (Shanghai, China). All reagents were analytical grade and deionized water was used throughout the experiment.

2. Experimental Setup

The water treatment experimental system of high-voltage pulsed streamer discharge for OG degradation is displayed in Fig. 1. The experimental system contains pulse power supply, reactor, electrical monitoring system and gas pipeline. The detailed information is given in the Supplementary Material.

3. Catalyst Preparation

β-Bi_2O_3 was prepared by the precipitation method followed by thermal treatment [16,17]. $CaFe_2O_4$ was synthesized by sol-gel method [18]. The detailed preparation methods of β-Bi_2O_3 and $CaFe_2O_4$ are given in the Supplementary Material. The composites of β-Bi_2O_3/$CaFe_2O_4$ were prepared by grinding and calcining method: 0.276 g β-Bi_2O_3 and 0.024 g $CaFe_2O_4$ were weighed and put into an agate mortar to mix and grind for 30 min. The obtained powder was washed with deionized water and anhydrous ethanol for three times and then dried at 60 °C. Finally, it was calcined in a muffle furnace at 350 °C for 90 min to obtain the β-Bi_2O_3/$CaFe_2O_4$ composite with 8.0 wt% $CaFe_2O_4$. By controlling the mass ratio of $CaFe_2O_4$ and β-Bi_2O_3, 5.0, 8.0, 12.0 and 15.0 wt% β-Bi_2O_3/$CaFe_2O_4$ composites were obtained, marked as CB-5, CB-8, CB-12 and CB-15.

4. Characterizations

The morphology and elemental composition of the samples were examined via scanning electron microscope (SEM, Hitachi, S-4800) and transmission electron microscopy (TEM, JEOL, JEM-F200).

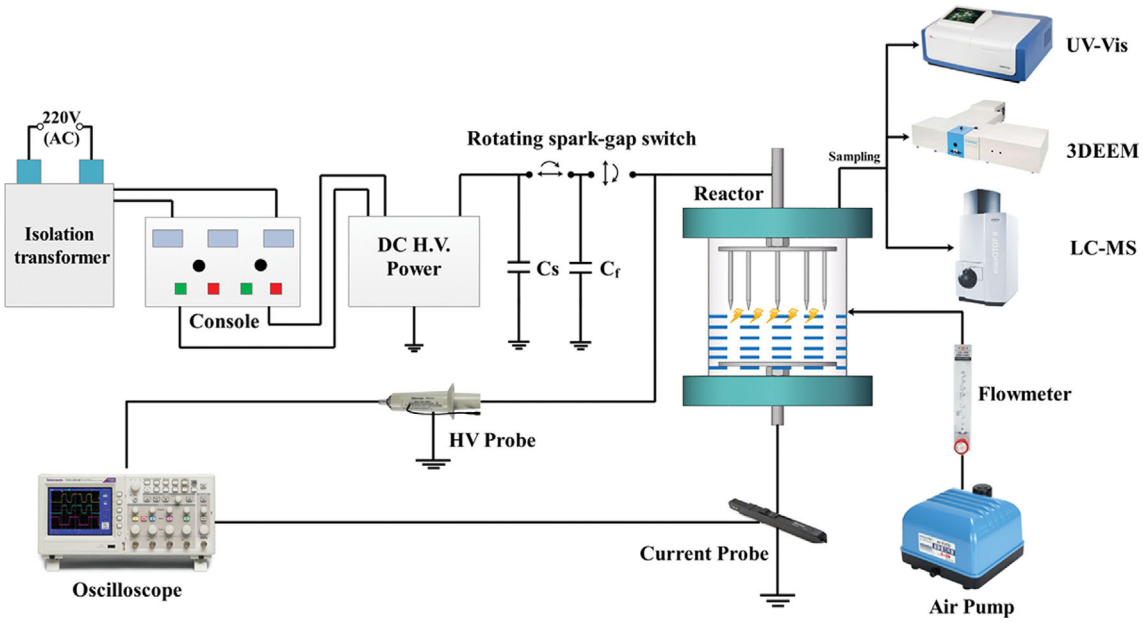

Fig. 1. Schematic experimental device of the OG degradation.

The crystal phases of the prepared samples were recorded by X-ray powder diffraction (XRD, Rigaku, MiniFlex600) with Cu Kα radiation. The Fourier transform infrared (FT-IR) spectrum of the obtained samples within the range of 4,000-400 cm^{-1} was determined on a Nicolet 6700 spectrometer (ThermoFisher, America). X-ray photoelectron spectroscopy (XPS) was monitored by Thermo ESCALAB-250XI.

5. Analytical Methods

The total amount, initial conductivity and initial concentration of OG solution were 80.0 mL, 79.0 μS/cm and 100.0 mg/L, respectively. The needle-liquid spacing and pulse frequency were kept at 4 mm and 42 Hz, respectively. KCl was used to adjust initial conductivity of OG solution, and the conductivity of OG solution was determined by conductivity meter (DDSJ-318, INESA, China). The concentration of liquid phase O_3 at the end of discharge was determined by the indigo method [27], and the concentration of H_2O_2 was determined by the potassium titanium oxalate colorimetric method [28]. Before discharge treatment, OG solution to be treated containing the catalyst was ultrasonicated dispersion in a dark environment for 30 min to ensure the catalysts were evenly dispersed in the solution. The catalyst dosage was 0.3 g/L. During discharge, the reaction solution was sampled with syringe needle at the intervals of 4 min. The concentration of OG solution was determined by UV-Vis spectrophotometer (L6S, INESA, China) after the samples were filtered with 0.22 μm syringe membrane filters. The detection wavelength was set as 478 nm [29]. Detailed evaluation indicators are available in the Supplementary Material. In addition, the extract solution after determination would return to the reactor to ensure the consistency of reaction capacity. Note that only CB-8 catalyst was added to the OG solution without plasma treatment resulting in the degradation efficiency of merely 2.0%. Three-dimensional fluorescence spectra of OG solution during the degradation were monitored by fluorescence spectrometer (Fluorolog-3, Jobin Yvon, America). The intermediates during OG degradation were detected by LC-MS (MicrOTOF-Q II, Bruker Daltonics, America), and the corresponding test condition is given in Supplementary Material.

RESULTS AND DISCUSSION

1. Characterization

Fig. 2(a), (b) and (c) display the morphologies of β-Bi_2O_3, $CaFe_2O_4$ and CB-8, respectively. It can be seen from Fig. 2(a) that β-Bi_2O_3 was mainly composed of aggregated nanorods and nanosheets with

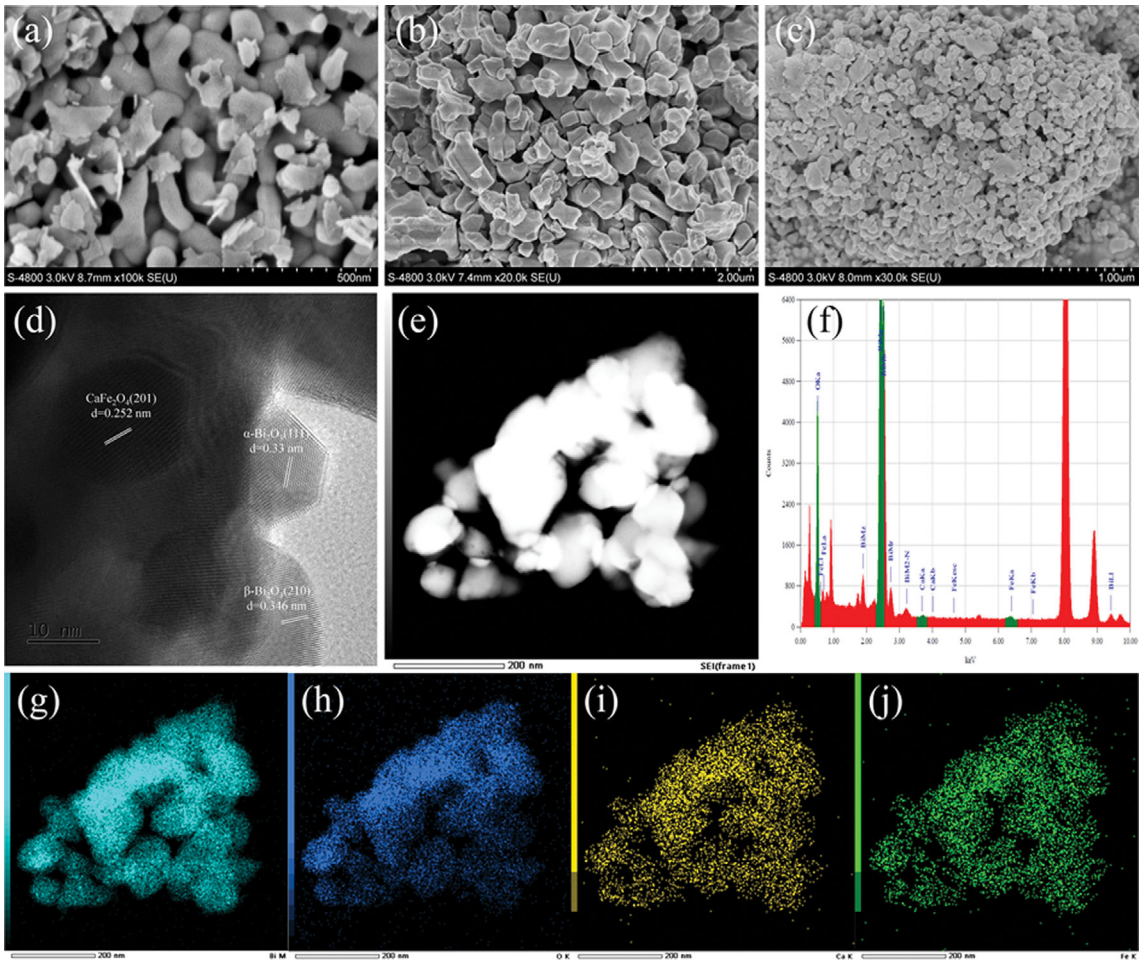

Fig. 2. SEM images of (a) β-Bi_2O_3, (b) $CaFe_2O_4$ and (c) CB-8; (d) HRTEM image of CB-8; (e) EDS electronic image of CB-8; (f) EDS of CB-8; (g) Bi, (h) O, (i) Ca and (j) Fe of EDS mapping images.

length and width ranging from 200 to 300 nm. Fig. 2(b) exhibits that the $CaFe_2O_4$ particles presented irregularly rectangular in shape and most of the particles agglomerated together. The composite nanoparticles of β-Bi_2O_3/$CaFe_2O_4$ were tightly connected to form an excellent heterojunction as shown in Fig. 2(c). TEM was used to analyze the microstructure of the composite. Fig. 2(d) depicts the HRTEM image of CB-8, in which the measured lattice spacing of 0.33 nm, 0.346 nm and 0.252 nm was consistent with the (111) plane of α-Bi_2O_3, (210) plane of β-Bi_2O_3 and (201) plane of $CaFe_2O_4$, respectively. The CB-8 composite contained the crystalline form of α-Bi_2O_3, manifesting that a part of β-Bi_2O_3 was converted to α-Bi_2O_3 during calcination of the composite. This is consistent with the XRD characterization of the composite. Fig. 2(e) presents the TEM image used for EDS scanning. The EDS diagram of CB-8 in Fig. 2(f) exhibits that the composite was composed of Bi, O, Ca and Fe elements. The EDS mapping images in Fig. 2(g), (h), (i) and (j) reveal that the four elements were basically evenly distributed on CB-8. Consequently, it can be deduced that CB-8 composites have been prepared successfully.

Fig. S1 exhibits the XRD patterns of β-Bi_2O_3, $CaFe_2O_4$ and CB-8 composite. The diffraction peaks of β-Bi_2O_3 at 2θ of 25.7°, 27.92°, 30.26°, 31.74°, 32.7°, 46.18° and 46.9° are assigned to the (210), (201), (211), (002), (220), (222) and (400) crystal planes of β-Bi_2O_3 (JCPDS: 27-0050), respectively. The peaks at 33.58°, 35.5°, 40.32° and 42.78° are attributed to diffractions of (320), (201), (131) and (311) planes of $CaFe_2O_4$ (JCPDS: 32-0168). Furthermore, the XRD pattern of CB-8 also contains the diffraction peaks of α-Bi_2O_3. The peaks at 24.58°, 26.88°, 27.42° and 33.24° correspond to (-102), (111), (120) and (200) crystal planes of α-Bi_2O_3 (JCPDS: 41-1449), suggesting that a part of β-Bi_2O_3 was converted to α-Bi_2O_3 under high temperature heat treatment. Due to the actual temperature in the chamber of the muffle furnace was higher than the set temperature and β phase is metastable state, if the treatment temperature exceeded 350 °C, β-Bi_2O_3 was gradually converted to monoclinic α-Bi_2O_3, which resulted in the crystalline diffraction of α-Bi_2O_3 in the composite spectrum [30,31]. This is consistent with the TEM results. HRTEM image displayed that lattice spacing of 0.346 nm and 0.252 nm of CB-8 were consistent with the (210) plane of β-Bi_2O_3 and (201) plane of $CaFe_2O_4$, respectively. The characteristics of diffraction peaks in CB-8 exhibited strong diffraction peaks of Bi_2O_3 (α and β phases) and weak diffraction peaks of $CaFe_2O_4$, which may be due to the less content of $CaFe_2O_4$ (8.0 wt%). The simultaneous appearance of the characteristic peaks indicated that the β-Bi_2O_3/$CaFe_2O_4$ composites were successfully prepared. The characteristic peak positions were not significantly shifted and the peaks were sharp, suggesting the good crystallinity of the composite samples. Moreover, the absence of impurity peaks in the spectra of the composite samples demonstrated that no other chemical reactions were involved in the binding process of the two species.

The FT-IR images of β-Bi_2O_3, $CaFe_2O_4$ and CB-8 are depicted in Fig. S2. For the three samples, the broad peak located at 3,442 cm^{-1} can be attributed to the O-H stretching vibration, while the peak located at 1,633 cm^{-1} can be assigned to the O-H bending vibration [32]. The absorption peaks at 1,368 cm^{-1} and 530 cm^{-1} in the β-Bi_2O_3 spectrum belong to the stretching vibration of the Bi-O bond [33]. The band at 876 cm^{-1} corresponds to Fe-Ca and bands at 640 and 452 cm^{-1} are attributed to Fe-O bonds due to the presence of ferrite skeleton in $CaFe_2O_4$ [19,34]. What is more, not only

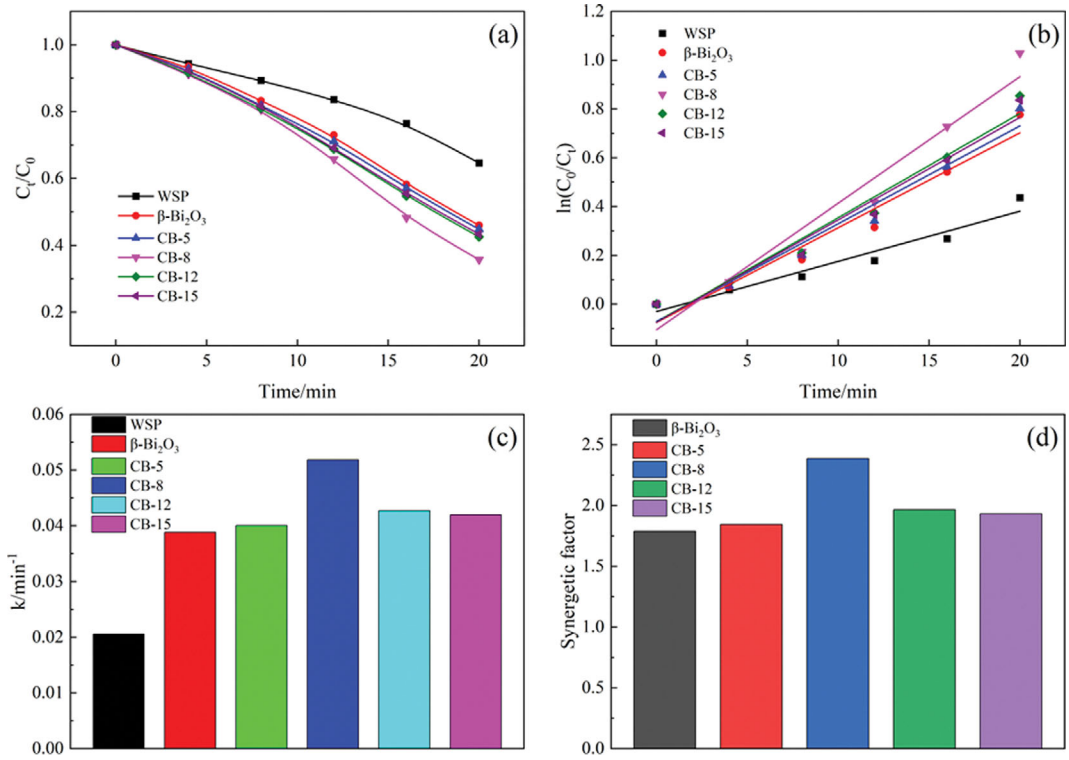

Fig. 3. Effect of the different catalyst on OG degradation: (a) degradation curves, (b) kinetic curves, (c) kinetic constants, (d) synergistic factors.

the vibrational modes of β-Bi_2O_3 but also those of $CaFe_2O_4$ were observed in the FT-IR spectrum of CB-8. This proves the coexistence of β-Bi_2O_3 and $CaFe_2O_4$ in the composite. To explore the chemical composition of the prepared samples in more depth, the results and analysis of the XPS characterization are presented in Fig. S3 of the Supplemental Material.

2. OG Degradation by WSP with Catalysts

The peak pulse voltage and air flow rate were 19.2 kV and 2.0 L/min, respectively. It can be seen from Fig. 3(a) that the OG removal efficiency of the WSP system alone was only 35.4% after 20 min of degradation when no catalyst was added. When β-Bi_2O_3 was added to WSP system, the removal efficiency reached 54.0% after 20 min of treatment, which was 18.6% higher than that of sole WSP. Compared with pure β-Bi_2O_3, the addition of β-Bi_2O_3/$CaFe_2O_4$ composites to WSP could further enhance OG degradation. In addition, the removal efficiency first enhanced and then declined with increasing the settling amount of $CaFe_2O_4$, reaching a maximum value of 64.3% when the settling amount was 8.0 wt%, which was 28.9% and 10.3% higher than that of sole WSP and WSP/β-Bi_2O_3, respectively. The kinetic curves and corresponding kinetic constants of OG degradation are displayed in Fig. 3(b) and (c). The fitting results exhibit that OG degradation in the WSP was in accordance with the pseudo-first-order reaction kinetics. The highest kinetic constant of 0.052 min^{-1} was obtained for the WSP/CB-8 system. Compared with WSP (0.021 min^{-1}) and WSP/β-Bi_2O_3 (0.039 min^{-1}), it was 2.48- and 1.33-times higher, suggesting that the addition of the composites can also improve the degradation rate of OG. This phenomenon was attributed to the addition of $CaFe_2O_4$ accelerating the separation rate of electron-hole pairs and improving the catalytic activity. However, excessive $CaFe_2O_4$ content will promote particle agglomeration due to its strong magnetic properties, accelerating particle sinking, and hinder the absorption of UV light by the catalyst, thus affecting the overall catalytic performance.

The synergistic factors of different systems are displayed in Fig. 3(d). Compared with pure β-Bi_2O_3, the synergistic factors of the WSP/composites combined system were higher, manifesting a more obvious synergistic effect. Besides, the synergistic factor of WSP/CB-8 system reached the maximum value of 2.387. Notably, all the synergistic factors were higher than 1, suggesting a synergistic effect between WSP and the catalyst.

3. Effect of Operational Factors on OG Degradation

3-1. Effect of Pulse Peak Voltage

The pulse peak voltage plays a vital role in the physicochemical effects generated by the discharge. As depicted in Fig. 4(a), the removal efficiency of OG increased with enhancing the peak voltage. The removal efficiency corresponding to peak voltages of 19.2, 21.0, 22.8, 24.6 and 26.4 kV were 64.3, 74.9, 87.0, 93.1 and 96.2% for 20 min of treatment, respectively. The inset Fig. 4(a) depicts the kinetic curves of OG degradation under different peak voltages, and the degradation process is in accordance with the pseudo-first-order

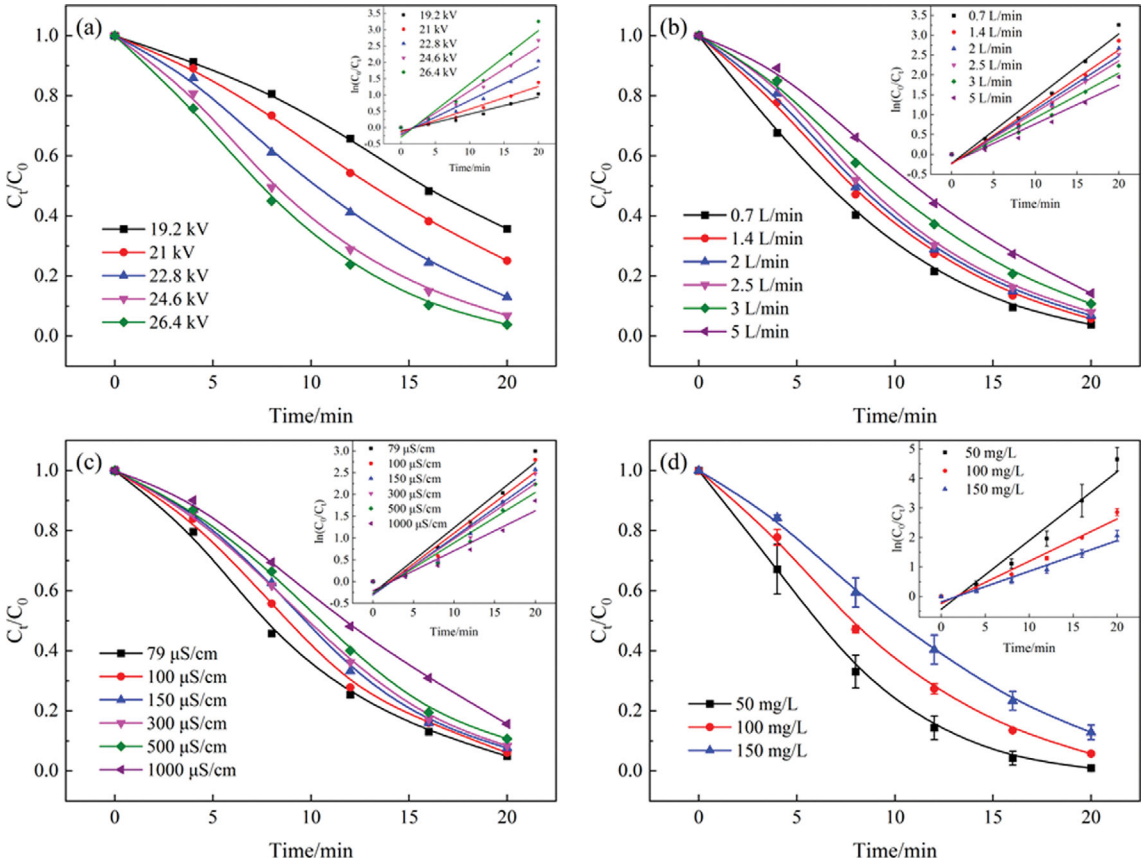

Fig. 4. Effect of operational factors on OG removal: (a) pulse peak voltage, (b) air flow rate, (c) initial conductivity of OG solution, (d) initial OG concentration.

reaction kinetics. Fig. S4(a) represents the kinetic constants with various peak voltages. The kinetic constant reached the maximum value of 0.163 min^{-1} when the peak voltage was 26.4 kV. This is because enhancing the peak voltage will strengthen the discharge intensity between the needle-plate electrodes and generate more active species to improve the OG removal. Furthermore, the high peak voltage enhanced the physical and chemical effects, which can be evidenced by the change of ion concentration in the solution. When the treatment time reached 20 min, the solution conductivity corresponding to the peak voltages of 19.2, 21.0, 22.8, 24.6 and 26.4 kV was 393 μS/cm, 432 μS/cm, 574 μS/cm, 673 μS/cm and 811 μS/cm, respectively. The significant increase of ion concentration suggested an enhancement in the input energy. It is noteworthy that the OG removal efficiency increased by only 3.1% when peak voltage was in the range of 24.6-26.4 kV, suggesting that it is uneconomical to blindly enhance the peak voltage in pursuit of high removal. Hence, the peak voltage was maintained at 24.6 kV.

3-2. Effect of Air Flow Rate

As shown in Fig. 4(b), the removal efficiency decreased gradually with enhancing air flow rate. The removal efficiency could reach 96.2% with 20 min treatment time at 0.7 L/min, while 95.0, 93.1, 91.9, 89.2 and 85.8% were achieved at 1.4, 2.0, 2.5, 3.0 and 5.0 L/min, respectively. The inset Fig. 4(b) exhibits the kinetic curves of OG degradation under different air flow rates, and the degradation process was in accordance with the pseudo-first-order kinetic model. Fig. S4(b) indicates the kinetic constants of OG degradation under different air flow rates, and the smaller air flow rate would accelerate the OG degradation. The corresponding kinetic constants were 0.163, 0.150, 0.135, 0.129, 0.113 and 0.098 min^{-1} for air flow rate of 0.7, 1.4, 2.0, 2.5, 3.0 and 5.0 L/min, respectively. This is because an excessively high air flow rate can severely accelerate the flow of gas molecules in the electric field, causing fewer oxygen molecules being dissociated. Besides, higher air flow rate will destroy the transfer balance and reduce the utilization of active species [35]. Nevertheless, lower air flow rate is not conducive to the release of heat in the reactor. Consequently, the air flow rate was maintained at 1.4 L/min.

3-3. Effect of Initial Conductivity of OG Solution

Fig. 4(c) presents the effect of initial conductivity of the solution on OG degradation in the WSP/CB-8 system. The OG removal efficiency decreased with enhancing initial conductivity of the OG solution. When the initial conductivity was 79.0, 100.0, 150.0, 300.0, 500.0 and 1,000.0 μS/cm, the removal efficiency was 95.0, 93.9, 92.4, 91.6, 89.3 and 84.4%, respectively. The removal efficiency could basically reach 90.0% when the initial conductivity increased to 500.0 μS/cm, indicating that the WSP/CB-8 system is suitable for treating wastewater with high conductivity. Furthermore, the OG removal efficiency decreased by only about 10.0% when the initial conductivity reached 1,000.0 μS/cm, demonstrating the potential application of this system to the treatment of industrial wastewater with high conductivity. The inset Fig. 4(c) demonstrates the OG degradation under different initial conductivity conforming to the pseudo-first-order reaction kinetics. The effect of initial conductivity of the solution on the kinetic constant is presented in Fig. S4(c). As the initial conductivity increased from 79.0 to 1,000.0 μS/cm, the kinetic constant decreased gradually from 0.150 min^{-1} to 0.092 min^{-1}. Apparently, the lower initial conductivity of the solution promoted the degradation of OG. The reason is attributed to that high conductivity raised ion concentration in the solution. Due to the conductive effect of ionic current in the solution with high conductivity, it was difficult to form a strong electric field. Moreover, the discharge intensity was weakened and the energy loss of the plasma input into the solution was accelerated, which weakened the generation of active species and thus hindered the OG degradation.

3-4. Effect of Initial OG Concentration

Fig. 4(d) depicts the effect of initial OG concentration on OG degradation in the WSP/CB-8 system. The OG removal efficiency gradually decreased with the increase of initial concentration. When the initial concentration was 50.0, 100.0 and 150.0 mg/L, the OG removal efficiency was 98.5, 95.0 and 84.4% after 20 min of treatment, respectively. Accordingly, the kinetic constants shown in Fig. S4(d) were 0.233, 0.143 and 0.104 min^{-1}, respectively. The inset Fig. 4(d) displays the OG degradation kinetic curves under different initial OG concentrations, and the degradation process is consistent with pseudo-first-order reaction kinetics. Apparently, the increase of initial OG concentration can induce the decline of removal efficiency and degradation rate of OG degradation. This is because the amount of energetic electrons and active species generated in the WSP/CB-8 system remains stable under a certain input energy. When the initial OG concentration was high, active species were not sufficient to degrade all the OG molecules, resulting in the decrease of OG removal efficiency.

4. Reuse Property of Catalysts

The repeatability and stability of catalysts are crucial for practical application. Therefore, the reuse performance of the CB-8 sample in WSP was evaluated. The peak voltage, catalyst dosage and air flow rate were controlled as 24.6 kV, 0.625 g/L and 2 L/min. As depicted in Fig. S5(a), the removal efficiency remained 90.8% after four degradation experiments, which was only 0.8% lower than the first use. Due to the catalyst dosage of 0.625 g/L (exceeding the optimum dosage) and the inevitable loss of catalyst after each experiment, the OG removal efficiency reached the maximum value in the second cycling test and then gradually declined. Besides, the XRD pattern of CB-8 after four consecutive cycles was almost identical to that of the fresh sample as revealed in Fig. S5(b). After four degradation experiments, CB-8 still had a high crystallinity. Therefore, the prepared CB-8 had good repeatability and stability.

5. Role of Active Species

For investigating the role of active species during OG removal, trapping experiments were performed for the possible free radicals. TBA, BQ, EDTA-2Na and KH_2PO_4 (MP) were utilized as scavengers for ·OH, $\cdot O_2^-$, h^+ and energetic electrons (e^{-*}), respectively. It can be seen from Fig. S6(a) that when TBA, EDTA-2Na, BQ and MP were added to the sole WSP, the removal efficiency of OG declined after 20 min of treatment, indicating that the four scavengers could inhibit the degradation of OG. TBA, BQ and MP reduced the removal efficiency of OG from 62.2% to 22.6%, 36.7% and 47.3%, respectively. Compared with no scavenger added, TBA, BQ and MP decreased the OG degradation efficiency by 39.6%, 25.5% and 14.9%, respectively. Consequently, it can be deduced that ·OH, e^{-*} and $\cdot O_2^-$ played a role in the OG degradation in WSP, and pulsed

discharge could generate e^{-*} and reactive species with high oxidation potentials, such as ·OH and $\cdot O_2^-$ (Eqs. (1)-(4)), which can react with organic pollutant molecules and induce their decomposition in a rapid, complete and non-selective manner [36,37].

$$H_2O + e^{-*} \rightarrow \bullet OH + \bullet H + e^- \quad (1)$$

$$H_2O + e^{-*} \rightarrow H_2O^+ + 2e^- \quad (2)$$

$$H_2O^+ + H_2O \rightarrow \bullet OH + H_3O^+ \quad (3)$$

$$e^{-*} + O_2 + M \rightarrow \bullet O_2^- + M \quad (4)$$

The addition of TBA, BQ and MP reduced the amount of active species in the WSP system and decreased the oxidation capacity of the reaction system. Therefore, these trapping agents hindered the decomposition of OG in the sole WSP. The decrease of removal efficiency in the WSP system after the addition of EDTA-2Na was owing to the increase in the initial conductivity of solution.

As illustrated in Fig. S6(b), the addition of all scavengers reduced the removal efficiency of OG in the WSP/CB-8 system. After adding TBA, EDTA-2Na, BQ and MP to the WSP/CB-8 system, the removal efficiency of OG decreased from 74.9% to 26.9%, 19.7%, 36.7% and 52.7% after 20 min of treatment, and the decline range was 48.0%, 55.2%, 38.2% and 22.2%, respectively. Fig. S6(c) presents that the decline in removal efficiency was higher in the WSP/CB-8 system, indicating that ·OH, h^+, $\cdot O_2^-$ and e^{-*} play a vital role in the OG removal. During the catalytic process, h^+, $\cdot O_2^-$ and ·OH can be generated via the following reactions [38]:

$$Bi_2O_3 + plasma \rightarrow e^- + h^+ \quad (5)$$

$$CaFe_2O_4 + plasma \rightarrow e^- + h^+ \quad (6)$$

$$H_2O + h^+ \rightarrow \bullet OH + H^+ \quad (7)$$

$$e^- + O_{2(aq.)} \rightarrow \bullet O_2^- \quad (8)$$

$$e^- + O_3 \rightarrow \bullet O_3^- \quad (9)$$

$$\bullet O_3^- + H^+ \rightarrow \bullet OH + O_2 \quad (10)$$

It has been demonstrated that e^{-*} generated via discharge has the mean electron energy of 1-25 eV, which could excite the photocatalysts with the band gap energy of 0.1-5 eV and achieve "pseudo photocatalysis" behavior [39]. Furthermore, the addition of MP also verified the role of e^{-*} for exciting the catalyst. It is evident that the addition of TBA, BQ, EDTA-2Na and MP could consume ·OH, $\cdot O_2^-$, h^+ and e^{-*} in the system, resulting in the lower OG removal efficiency.

6. Formation of H_2O_2 and O_3

The concentrations of H_2O_2 and O_3 in the water samples at 20 min of treatment under each system of sole WSP and WSP+catalyst were investigated, and the results are shown in Fig. S7. As shown in Fig. S7(a), the H_2O_2 concentration of OG solution (0.096 mmol/L) was much lower than that of deionized water (0.626 mmol/L) in the WSP system, suggesting that the degradation of OG consumed H_2O_2. Similarly, the H_2O_2 concentration of OG solution (0.187 mmol/L) was smaller than that of deionized water (0.738 mmol/L) in the WSP+catalyst system. This implies that H_2O_2 played a role in the degradation of OG under both reaction systems. It is noteworthy that regardless of whether the water sample to be treated was deionized water or OG solution, the concentration of H_2O_2 in the WSP+catalyst system was higher after 20 min of treatment. The reason is attributed to that the yield of ·OH improved due to the addition of catalyst, which increased the concentration of H_2O_2. Besides, ·OH has the extremely short lifetime and can rapidly recombine to form H_2O_2 [40]:

$$\bullet OH + \bullet OH + M \rightarrow H_2O_2 + M \quad (11)$$

It can be seen from Fig. S7(b) that no matter with or without the addition of catalyst, the concentration of O_3 in OG solution was lower at 20 min of discharge, demonstrating that O_3 played a certain role in the degradation of OG. In the WSP system, O_3 is mainly generated through the following ways [41]:

$$O_2 + e^{-*} \rightarrow 2\bullet O + e^- \quad (12)$$

$$O_2 + \bullet O + M \rightarrow O_3 + M \quad (13)$$

In addition, it can be noticed that no matter whether the water sample to be treated was deionized water or OG solution, the concentration of O_3 generated by the WSP+catalyst system was higher than that in the sole WSP system after 20 min of treatment, suggesting that the combined system contributes to the generation of O_3.

7. Three-dimensional Fluorescence Analysis

Three-dimensional fluorescence properties are closely related to the molecular structure and functional groups, which was therefore used to analyze the transformation process of molecular structures during the degradation of OG. The excitation wavelength and emission wavelength were scanned in the ranges of 250-400 nm and 300-650 nm, respectively. The 3DEEM fluorescence spectra of OG solution under different treatment time during the degradation are presented in Fig. 5. As depicted in Fig. 5(a), there were four kinds of fluorescence peaks at Ex/Em=(280-310 nm)/(525-550 nm), Ex/Em=(270-310 nm)/(425-450 nm), Ex/Em=(330-350 nm)/(525-550 nm) and Ex/Em=(330-350 nm)/(425-450 nm) in the untreated OG solution. The intensity of the fluorescence peaks located in the region of Ex/Em=(280-310 nm)/(525-550 nm) was significantly reduced, which was due to the gradual decomposition of OG molecules (shown in Fig. 5(b)). Moreover, the intensity of the characteristic peaks was further weakened with the enhancement of degradation time, resulting in the disappearance of fluorescence peaks and appearance of new fluorescence peaks. This indicates that the conjugated heterocyclic structure of OG was destroyed and different intermediates were formed, as presented in Fig. 5(c) and (d). During the degradation process, the azo bond of the OG molecule was broken to form monocyclic aromatic compounds and naphthalene ring compounds with strong fluorescence properties, which enhanced the fluorescence intensity of the system as well as the blue shift of the fluorescence peak [42]. Accordingly, the 3DEEM spectra before and after the treatment further confirmed that the WSP/CB-8 system was able to destroy the OG molecular structure.

8. Intermediates and Possible Degradation Pathway

The degradation intermediates of OG molecule generated in the WSP/CB-8 system were identified by LC-MS, and 13 intermediates (listed in Table S1) could be determined. The mass spectra of intermediates are given in Fig. S8. The targets of radical attack

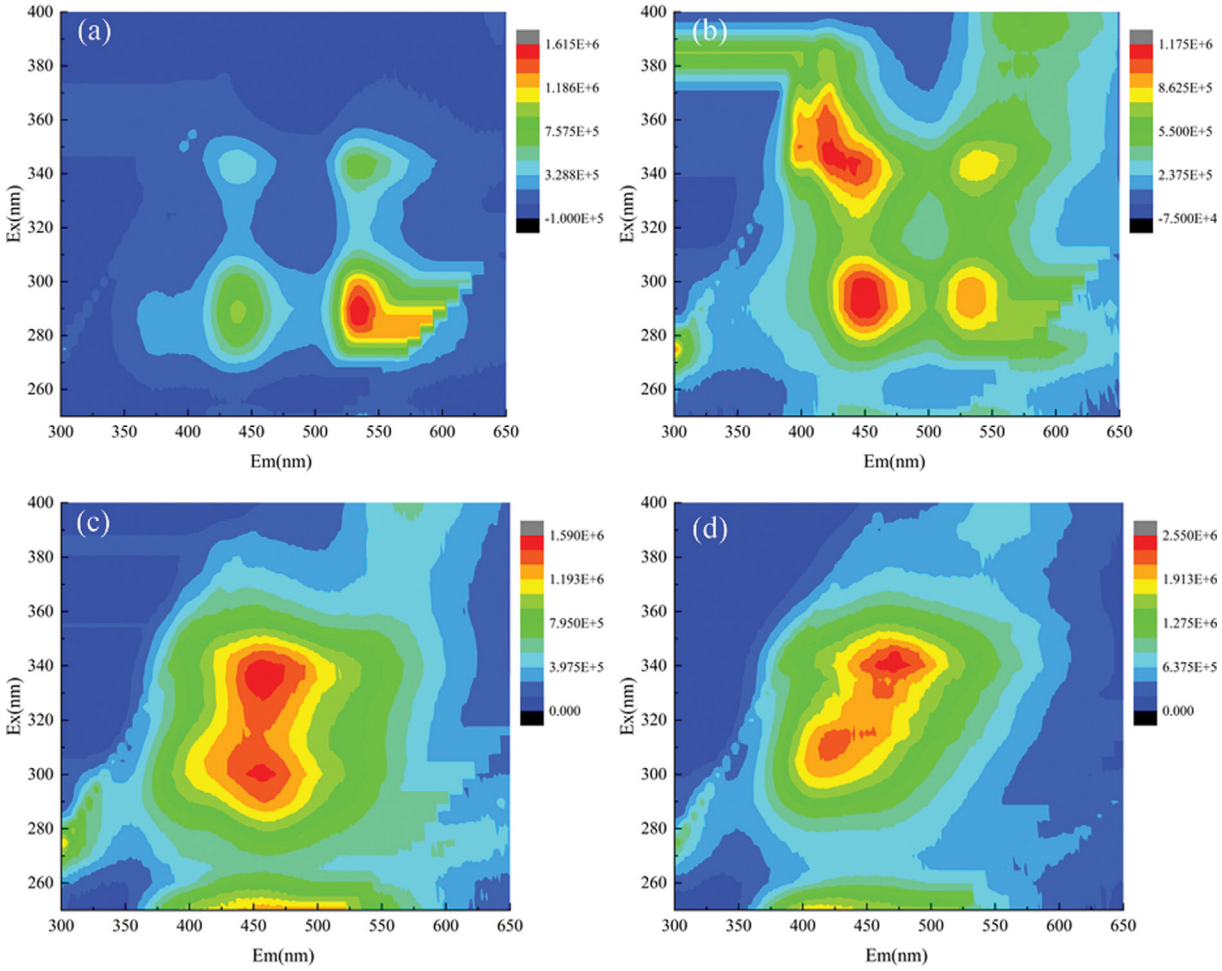

Fig. 5. Three-dimensional fluorescence spectra of OG solution at different degradation times: (a) 0 min, (b) 6 min, (c) 13 min, (d) 20 min.

are mainly the electron rich π bonds of the azo group, the sulfonate group and to a lesser extent the partially deactivated aromatic ring [43]. Three possible degradation pathways of OG displayed in Fig. 6 were proposed, resulting from the indiscriminate attack of ·OH radical at different sites on the OG dye molecule.

As presented in Pathway I of Fig. 6, since the sulfonate functional group was sensitive to ·OH, the OG molecule lost the sulfonate group (-SO_3H) under the attack of ·OH to generate 7-hydroxy-8-azophenyl-naphthalene-1-sulfonic acid (P1, MW=328). Subsequently, hydroxyl radical attacked the naphthalene ring (addition or removal) to form the intermediate P3 (MW=312) and P4 (MW=342). Hydroxyl radical attacked aromatic ring to form hydroxy compounds. The intermolecular dehydration finally formed 7-oxy-8-azo-naphthalene-(1′-oxy-2′-azo-phenyl)-1-sulfonic acid (P2, MW=326) [44]. Another possible pathway is depicted in Pathway II of Fig. 6. Previous research confirmed that the azo chromophore is the essential functional group responsible for the color of azo dye [45]. For OG molecules, the conjugated system of azo double bonds (-N=N-) is most vulnerable to the damage of ·OH, rather than directly attacking the aromatic ring. The strong oxidizing ·OH attacked the bond between the nitrogen atom and benzene ring in the azo double bond, and the azo bond was oxidatively cleaved to generate the intermediate P5 (MW=364), which lost the sulfonate group to form P6 (MW=284). Next, ·OH was added to the aromatic ring to form hydroxyaromatic amine P7 (MW=204).

The other probable pathway is also exhibited in Pathway III of Fig. 6. Under the attack of hydroxyl radical, the azo bond was cleaved to generate aniline and intermediate P8 (MW=335). On the one hand, the central atom of the sulfonate functional group was susceptible to the attack of ·OH radical, leading to the formation of intermediate P9 (MW=239). Subsequently, α-hydroxy compound was produced under the similar pattern of ·OH radical attack, elimination and bond cleavage, which was further oxidized and cleaved to yield dicarboxylic acid (P10, MW=225) [43]. Eventually, phthalic acid (P11, MW=166) was formed. On the other hand, intermediate P8 lost sulfonate group and cleaved into hydroxylamines, leading to the formation of intermediates P12 (MW=255) and P13 (MW=175). With the continuation of cleavage and oxidation, the intermediates decomposed and converted into organic acids with small molecules, inorganic acid ions, CO_2 and H_2O.

9. Comparison of WSP/CB-8 with other AOPs for OG Degradation

The removal of OG by WSP/CB-8 in this study was compared with other AOPs in the literature based on the initial OG concentration, reaction time, removal efficiency and reaction rate constant, which is displayed in Table 1. Zhao et al. [46] employed electro-

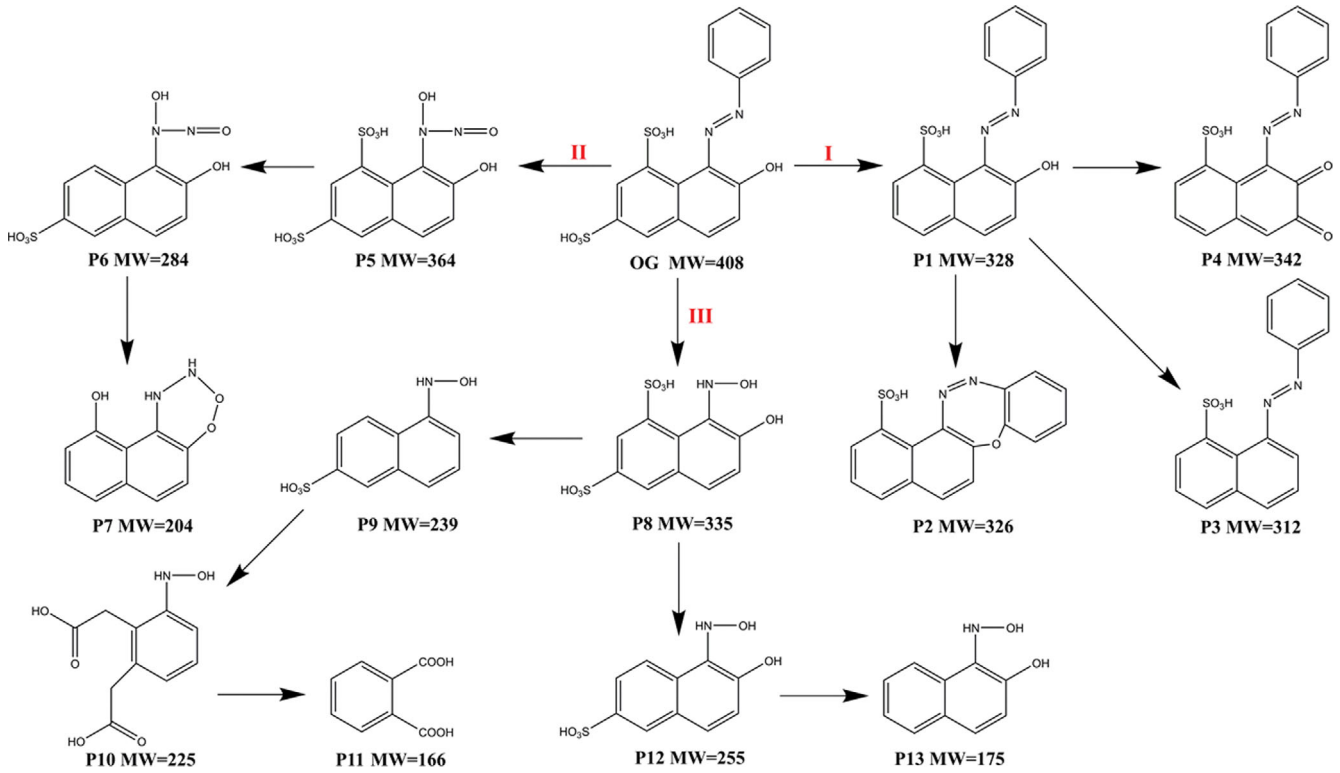

Fig. 6. Possible degradation pathway of OG in WSP/CB-8 system.

Table 1. Comparison of WSP/CB-8 with other competitive methods for OG degradation

AOPs	OG concentration	Reaction time (min)	Removal efficiency (%)	Reaction rate constant	Reference
Electrochemical	200 mg/L	240	98.6	Not reported	[46]
Sonophotocatalysis	0.09 mM	75	85.0	22.3×10^{-7} M min^{-1}	[47]
Fenton-like	100 mg/L	120	99.7	0-1 h: 1.1590 h^{-1} 1-2 h: 4.5531 h^{-1}	[48]
Titanium aminophosphates/H_2O_2	1.0×10^{-3} M	250	97.3	Not reported	[49]
Photocatalytic	10 mg/L	60	94.0	4.23×10^{-2} min^{-1}	[50]
Activated persulfate	0.2 mM	40	95.0	Not reported	[51]
gliding arc plasma/laterite soil	0.1 mM	60	100.0	0.186-0.076 min^{-1} for 0.05-0.15 mM	[52]
WSP/CB-8	100 mg/L	20	96.2	0.163 min^{-1}	Present study

chemical technology for the degradation of OG. The removal efficiency reached 98.6% after 240 min of treatment with the initial OG concentration of 200 mg/L. However, the concern is that the reaction time was relatively long. Madhavan et al. [47] used a combination of ultrasound and photocatalysis to degrade OG in aqueous solution. In the case of high input, the degradation efficiency needs to be improved. Fenton-like [48] and H_2O_2 oxidation [49] are common AOPs used for the degradation of organic contaminants. Although the degradation efficiency was relatively high, there were drawbacks of longer processing time and lower reaction rate. Barzgari et al. [50] applied Mn-doped ZnO catalyst to degrade OG. The removal efficiency of OG was 94% within 60 min with an initial OG concentration of 10 mg/L. However, the reaction rate constant for OG degradation was just 4.23×10^{-2} min^{-1}. Lin et al. [51] employed $FeMoO_4$ to activate persulfate for OG degradation. The removal efficiency of OG solution with an initial concentration of 0.2 mM reached 95% after 40 min of reaction. Tarkwa et al. [52] reported that gliding arc plasma was coupled with laterite soil for the OG degradation. 100% decolorization was achieved after 60 min treatment time of OG solution with the initial concentration of 100 mg/L. Besides, the kinetic constants decreased from 0.186 min^{-1} to 0.076 min^{-1} when the initial OG concentration was enhanced from 0.05 mM to 0.15 mM, respectively. In our study, a novel method of WSP coupled with β-Bi_2O_3/$CaFe_2O_4$ composites for synergistic degradation of dye wastewater with high concentration was proposed. The removal efficiency of OG in aqueous solu-

tion with an initial concentration of 100 mg/L for 20 min treatment could reach 96.2%. The kinetic constant of the degradation process was 0.163 min^{-1}. As is evident from the results, for the remediation of OG wastewater, the WSP/CB-8 system can not only ensure high degradation efficiency, but also shorten the treatment time and improve the degradation rate. Furthermore, the combined system is applicable for the remediation of wastewater with high conductivity (1,000.0 μS/cm), demonstrating the potential application for handling industrial wastewater with high conductivity, which is beneficial for industrial applications of non-thermal plasma in the field of practical wastewater treatment.

CONCLUSION

A new method was developed of WSP combining with β-Bi_2O_3/$CaFe_2O_4$ composites for the degradation of OG in aqueous solution. The characterization results demonstrated the successful preparation of the obtained composites. The addition of composites improved the removal efficiency, kinetic constant and synergistic factor of OG degradation in the WSP system, and the CB-8 sample exhibited a better synergistic effect. The peak pulse voltage of 24.6 kV and air flow rate of 1.4 L/min facilitated OG degradation. The lower initial solution conductivity and initial solution concentration favored OG removal. Furthermore, the WSP/CB-8 system was suitable for the remediation of wastewater with high conductivity. CB-8 catalyst exhibits good stability and reusability. ·OH, h^+, $\cdot O_2^-$ and e^{-*} devoted to OG removal in the WSP/CB-8 system, and the generated O_3 and H_2O_2 were also involved in OG removal. Three-dimensional fluorescence demonstrated that the OG molecules were disrupted and a variety of intermediates were generated. There were 13 intermediates that could be detected by LC-MS and three possible degradation pathways of OG were proposed. Compared with other methods for OG degradation, the WSP/CB-8 system has the advantages of high efficiency, fast reaction and short time consuming. The coupling of WSP with CB-8 catalyst for efficient remediation of high-conductivity industrial wastewater is expected to become a promising technology.

SUPPORTING INFORMATION

Additional information as noted in the text. This information is available via the Internet at http://www.springer.com/chemistry/journal/11814.

REFERENCES

1. M. Caldera-Villalobos, A. A. Pelaez-Cid, M. A. Martins-Alho and A. M. Herrera-Gonzalez, *Korean J. Chem. Eng.*, **35**, 2394 (2018).
2. S. Singh, R. Sharma and M. Khanuja, *Korean J. Chem. Eng.*, **35**, 1955 (2018).
3. A. Ajmal, I. Majeed, R. N. Malik, H. Idriss and M. A. Nadeem, *RSC Adv.*, **4**, 37003 (2014).
4. R. Zhang, Q. H. He, Y. Huang and X. T. Wang, *Arch. Biochem. Biophys.*, **596**, 1 (2016).
5. J. W. Yoon, M. H. Baek, J. S. Hong, C. Y. Lee and J. K. Suh, *Korean J. Chem. Eng.*, **29**, 1722 (2012).
6. A. R. Rahmani, K. Godini, D. Nematollahi, G. Azarian and S. Maleki, *Korean J. Chem. Eng.*, **33**, 532 (2016).
7. C. G. Joseph, Y. H. Taufiq-Yap, N. A. Affandi, J. L. H. Nga and V. Vijayan, *Korean J. Chem. Eng.*, **39**, 484 (2022).
8. K. F. Shang, J. Y. Ren, Q. Zhang, N. Lu, N. Jiang and J. Li, *J. Environ. Chem. Eng.*, **9**, 105767 (2021).
9. W. J. Hua and Y. Kang, *Sep. Purif. Technol.*, **279**, 119691 (2021).
10. Y. S. Mok and J. O. Jo, *Korean J. Chem. Eng.*, **24**, 607 (2007).
11. B. Jiang, J. T. Zheng, Q. Liu and M. B. Wu, *Chem. Eng. J.*, **204-206**, 32 (2012).
12. K. F. Shang, J. Li, X. J. Wang, D. Yao, N. Lu, N. Jiang and Y. Wu, *Jpn. J. Appl. Phys.*, **55**, 01AB02 (2015).
13. J. Jose and L. Philip, *J. Environ. Sci.*, **101**, 382 (2021).
14. M. Sato, T. Tokutake, T. Ohshima and A. T. Sugiarto, *IEEE Trans. Ind. Appl.*, **44**, 1397 (2008).
15. D. Luo and Y. Kang, *J. Mater. Sci.*, **54**, 1549 (2019).
16. X. D. Tang, Z. R. Wang, N. Wu, S. L. Liu and N. Liu, *Catal. Commun.*, **119**, 119 (2019).
17. S. Q. Han, J. Li, K. L. Yang and J. Lin, *Chin. J. Catal.*, **36**, 2119 (2015).
18. D. Luo and Y. Kang, *Mater. Lett.*, **225**, 17 (2018).
19. S. Vadivel, D. Maruthamani, A. Habibi-Yangjeh, B. Paul, S. S. Dhar and K. Selvam, *J. Colloid Interface Sci.*, **480**, 126 (2016).
20. M. G. Ahmed, T. A. Kandiel, A. Y. Ahmed, I. Kretschmer, F. Rashwan and D. Bahnemann, *J. Phys. Chem. C*, **119**, 5864 (2015).
21. H. Y. Jiang, P. Li, G. G. Liu, J. H. Ye and J. Lin, *J. Mater. Chem. A*, **3**, 5119 (2015).
22. J. Kim, C. W. Lee and W. Choi, *Environ. Sci. Technol.*, **44**, 6849 (2010).
23. K. F. Shang, J. Li and R. Morent, *Plasma Sci. Technol.*, **21**, 043001 (2019).
24. H. Akiyama and M. Akiyama, *IEEJ Trans. Electr. Electron. Eng.*, **16**, 6 (2021).
25. P. Hoffer, Y. Sugiyama, S. H. R. Hosseini, H. Akiyama, P. Lukes and M. Akiyama, *J. Phys. D-Appl. Phys.*, **49**, 415202 (2016).
26. Ruma, H. Hosano, T. Sakugawa and H. Akiyama, *Catalysts*, **8**, 213 (2018).
27. H. Bader and J. Hoigné, *Water Res.*, **15**, 449 (1981).
28. R. M. Sellers, *Analyst*, **105**, 950 (1980).
29. W. J. Sang, W. Lu, L. J. Mei, D. N. Jia, C. Cao, Q. Li, C. Wang, C. Zhan and M. Li, *Sep. Purif. Technol.*, **277**, 119473 (2021).
30. K. K. Bera, R. Majumdar, M. Chakraborty and S. K. Bhattacharya, *J. Hazard. Mater.*, **352**, 182 (2018).
31. R. P. Hu, X. Xiao, S. H. Tu, X. X. Zuo and J. M. Nan, *Appl. Catal., B*, **163**, 510 (2015).
32. V. H. Nguyen, M. Mousavi, J. B. Ghasemi, Q. Van Le, S. A. Delbari, A. S. Namini, M. S. Asl, M. Shokouhimehr and M. Mohammadi, *J. Phys. Chem. C*, **124**, 27519 (2020).
33. F. Kargar, A. Bemani, M. H. Sayadi and N. Ahmadpour, *J. Photochem. Photobiol., A*, **419**, 113453 (2021).
34. L. Khanna and N. K. Verma, *Phys. B*, **427**, 68 (2013).
35. H. Guo, Y. W. Wang, X. Yao, Y. T. Zhang, Z. Li, S. J. Pan, J. G. Han, L. J. Xu, W. C. Qiao, J. Li and H. J. Wang, *Chem. Eng. J.*, **425**, 130614 (2021).
36. M. A. Malik, A. Ghaffar and S. A. Malik, *Plasma Sources Sci. Technol.*, **10**, 82 (2001).
37. B. Jiang, J. T. Zheng, S. Qiu, M. B. Wu, Q. H. Zhang, Z. F. Yan and

Q. Z. Xue, *Chem. Eng. J.*, **236**, 348 (2014).
38. H. Guo, Z. Li, L. R. Xiang, N. Jiang, Y. Zhang, H. J. Wang and J. Li, *J. Hazard. Mater.*, **403**, 123673 (2021).
39. H. Guo, N. Jiang, H. J. Wang, N. Lu, K. F. Shang, J. Li and Y. Wu, *J. Hazard. Mater.*, **371**, 666 (2019).
40. F. Bilea, C. Bradu, N. B. Mandache and M. Magureanu, *Chemosphere*, **236**, 124302 (2019).
41. R. K. Singh, V. Babu, L. Philip and S. Ramanujam, *J. Water Process Eng.*, **11**, 118 (2016).
42. K. L. Sun, D. Yuan, Y. Liu, Y. Son, Z. Q. Sun and R. T. Liu, *Sep. Sci. Technol.*, **55**, 3175 (2020).
43. M. A. Meetani, M. A. Rauf, S. Hisaindee, A. Khaleel, A. AlZamly and A. Ahmad, *RSC Adv.*, **1**, 490 (2011).
44. M. Q. Cai, M. C. Jin and L. K. Weavers, *Ultrason. Sonochem.*, **18**, 1068 (2011).
45. J. Zhang, M. Y. Chen and L. Zhu, *RSC Adv.*, **6**, 758 (2016).
46. R. Y. Zhao, Y. M. Wang, J. Li, W. H. Meng, C. L. Yang, C. X. Sun and X. F. Lan, *J. Appl. Electrochem.*, **52**, 573 (2022).
47. J. Madhavan, F. Grieser and M. Ashokkumar, *Ultrason. Sonochem.*, **17**, 338 (2010).
48. J. H. Park, J. J. Wang, R. Xiao, N. Tafti, R. D. DeLaune and D. C. Seo, *Bioresour. Technol.*, **249**, 368 (2018).
49. A. Rajini, M. Nookaraju, S. Chirra, A. K. Adepu and N. Venkatathri, *RSC Adv.*, **5**, 106509 (2015).
50. Z. Barzgari, A. Ghazizadeh and S. Z. Askari, *Res. Chem. Intermed.*, **42**, 4303 (2016).
51. X. M. Lin, Y. W. Ma, J. Q. Wan, Y. Wang and Y. T. Li, *Chemosphere*, **214**, 642 (2019).
52. J. B. Tarkwa, E. Acayanka, B. Jiang, N. Oturan, G. Y. Kamgang, S. Laminsi and M. A. Oturan, *Appl. Catal., B*, **246**, 211 (2019).

Supporting Information

Synergistic degradation of Orange G in water via water surface plasma assisted with β-Bi_2O_3/$CaFe_2O_4$

Weijie Hua and Yong Kang†

School of Chemical Engineering and Technology, Tianjin University, Tianjin 300350, China
(*Received 3 July 2022 • Revised 10 August 2022 • Accepted 30 August 2022*)

EXPERIMENTAL

1. Experimental Setup

The experimental system was composed of high-voltage pulse power supply, discharge reactor, electrical detection system, air pump and its pipeline. The high-voltage pulse power supply (DGM-30, Dalian Power Technology Co., Ltd, China) consisted of isolation transformer, console, DC high-voltage power supply and rotating spark gap, which output positive and negative alternating bidirectional pulse. The pulse peak voltage and pulse frequency were 0-±35 kV and 0-200 pulses per second (pps) adjustable, respectively. The rise time was less than 50 ns and pulse-forming capacitor C_f was 5,600 pf. The discharge voltage and current were monitored via a digital oscilloscope (TDS2024C, Tektronix) equipped with a high-voltage probe (P6015A, Tektronix) and a current probe (P6021A, Tektronix). The reactor had an inner diameter of 70 mm and a height of 80 mm, which was made of cylindrical Plexiglass. The electrode structure was in the form of multi-needle-to-plate. The needle electrode was discharge electrode, which was composed of five titanium (TA2) needles. The needle electrodes were located in the gas phase over the water surface. The ground electrode was located at the bottom of the reactor, which was composed of a circular titanium plate with the diameter of 60 mm and thickness of 2 mm. An air pump (V-20, Hailea, China) was used to inject air into the discharge reactor. The inlet position was at the same height as the needle tip, and the air flow rate was adjusted by flowmeter (LZB-4WB(F), Shuanghuan, China).

2. Catalyst Preparation

β-Bi_2O_3 was prepared by precipitation and thermal treatment. First, 12 mmol of $Bi(NO_3)_3{\cdot}5H_2O$ was dissolved in 30 mL of HNO_3 (1 mol/L) solution. Subsequently, 120 mL of Na_2CO_3 (0.6 mol/L) solution was added dropwise to the above solution under sufficient stirring. The obtained suspension was further stirred for 60 min. The suspension was filtered and the separated precipitate was washed with deionized water and absolute ethanol, followed by drying at 70 °C for 3 h to obtain a white $Bi_2O_2CO_3$ precursor. Then, $Bi_2O_2CO_3$ was calcined at 350 °C for 90 min to obtain deep yellow β-Bi_2O_3.

$CaFe_2O_4$ was synthesized by sol-gel method: 4.723 g of $Ca(NO_3)_2{\cdot}4H_2O$, 16.160 g of $Fe(NO_3)_3{\cdot}9H_2O$ and 8.406 g of citric acid were added into 20 mL deionized water and the mixed solution was stirred magnetically for 60 min, then 8 mL ethylene glycol was added to continue stirring for 30 min. The transparent solution was placed at 80 °C with stirring and heated to evaporate the water, and the obtained polymer gel was dried at 80 °C for 24 h. Then it was placed in a muffle furnace at 350 °C for 2 h to obtain the $CaFe_2O_4$ precursor by pyrolysis and polycondensation. Finally, $CaFe_2O_4$ powder was obtained by heat treatment at 850 °C for 3 h.

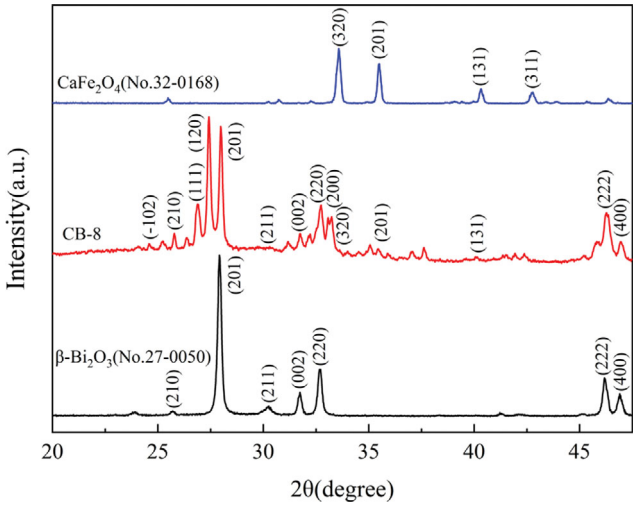

Fig. S1. XRD patterns of β-Bi_2O_3, $CaFe_2O_4$ and CB-8 composite.

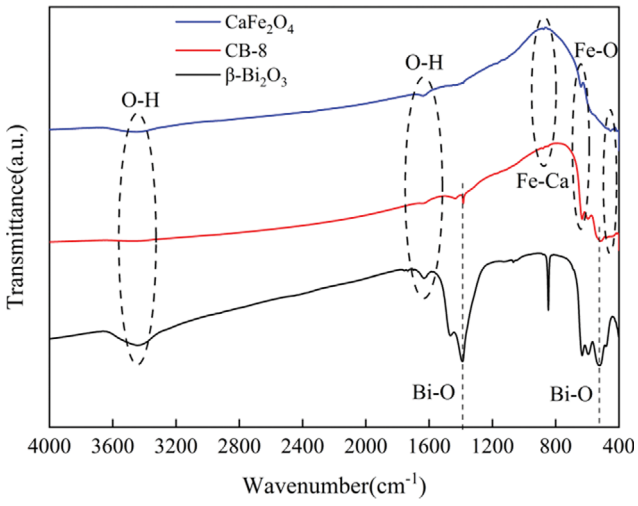

Fig. S2. FT-IR patterns of β-Bi_2O_3, $CaFe_2O_4$ and CB-8 composite.

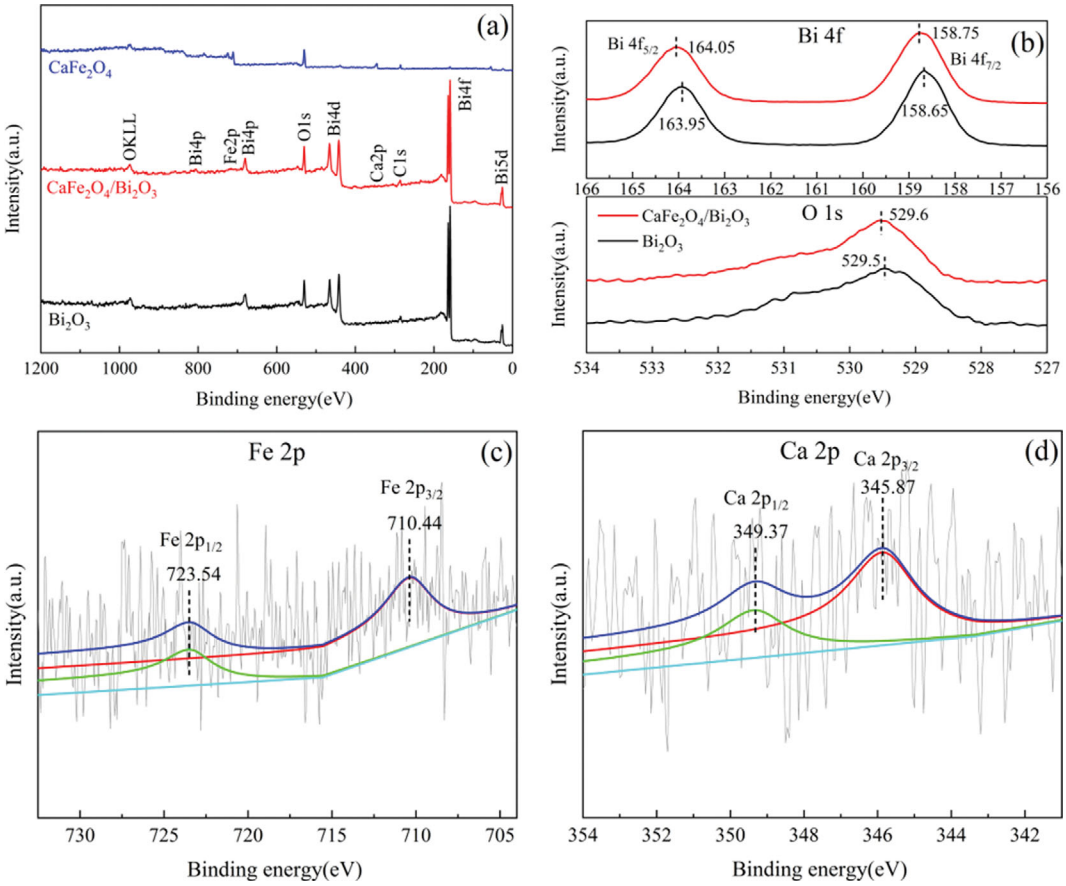

Fig. S3. (a) XPS full spectrum of Bi_2O_3, $CaFe_2O_4$ and $CaFe_2O_4/Bi_2O_3$; High-resolution XPS spectra of (b) Bi 4f and O 1s, (c) Fe 2p and (d) Ca 2p in CB-8 composite.

3. Analytical Methods

The degradation efficiency of OG was calculated as follows:

$$\eta = \frac{C_0 - C_t}{C_0} \quad \text{(S1)}$$

Where C_0 is the initial concentration of OG, mg/L; C_t is the concentration of OG at t min, mg/L. The kinetic of OG degradation was analyzed according to the pseudo-first-order kinetic model:

$$\ln\left(\frac{C_0}{C_t}\right) = kt \quad \text{(S2)}$$

Where the definitions of C_0 and C_t are the same as Eq. (1); k is the kinetic constant, min^{-1}; t is the reaction time, min.

To illustrate the synergistic effect between WSP and catalyst, the synergistic factor (SF) was defined according to the kinetic constant:

$$SF = \frac{k(WSP + catalyst)}{k(WSP) + k(catalyst)} \quad \text{(S3)}$$

Where k(WSP+catalyst) is the kinetic constant of OG degradation via WSP with catalyst; k(WSP) is the kinetic constant of sole WSP treatment; k(catalyst) is the kinetic constant of sole catalyst addition, 0.00116 min^{-1}.

The degradation intermediates of OG were identified by liquid chromatography-mass spectrometry (LC-MS) on Agilent 1200 HPLC with electrospray ionization quadrupole time-of-flight mass spectrometry (Bruker Daltonics, MicrOTOF-Q II) and separated by an Agilent Eclipse Plus C18 column (3.5 μm, 150×2.1 mm). The samples were filtered through 0.22 μm membrane filter before detection. The elution was performed via 0.1% (v/v) of formic acid aqueous solution (A) and acetonitrile (B) at the flow rate of 0.2 mL/min. The injection volume was 5 μL and the column temperature was set at 30 °C. MS was performed in the positive ion mode using electrospray ionization (ESI) source under the following conditions: m/z range 50-2,000, capillary voltage 4.5 kV, drying gas (N_2) flow rate 6 L/min, drying gas temperature 180 °C, and using sodium formate standard solution for online calibration.

4. XPS Analysis

The XPS full spectra of β-Bi_2O_3, $CaFe_2O_4$ and CB-8 are depicted in Fig. S3(a). The presence of Bi, O, Fe and Ca elements was detected in the full spectra of composite, where the C 1s binding energy was corrected at 284.80 eV. This demonstrates the successful recombination of Bi_2O_3 and $CaFe_2O_4$. Fig. S3(b) displays the fine scanning spectrum of Bi 4f and O 1s in Bi_2O_3 and $CaFe_2O_4/Bi_2O_3$. The strong peaks at 158.65 eV and 163.95 eV on the Bi 4f orbital corresponded to Bi $4f_{7/2}$ and Bi $4f_{5/2}$ of Bi^{3+} in Bi_2O_3, respectively [1]. The Bi $4f_{7/2}$ and Bi $4f_{5/2}$ orbitals in the composite were shifted to larger values (158.75 eV and 164.05 eV). The binding energy of O 1s in Bi_2O_3 was 529.5 eV, while in the composite was 529.6 eV [2].

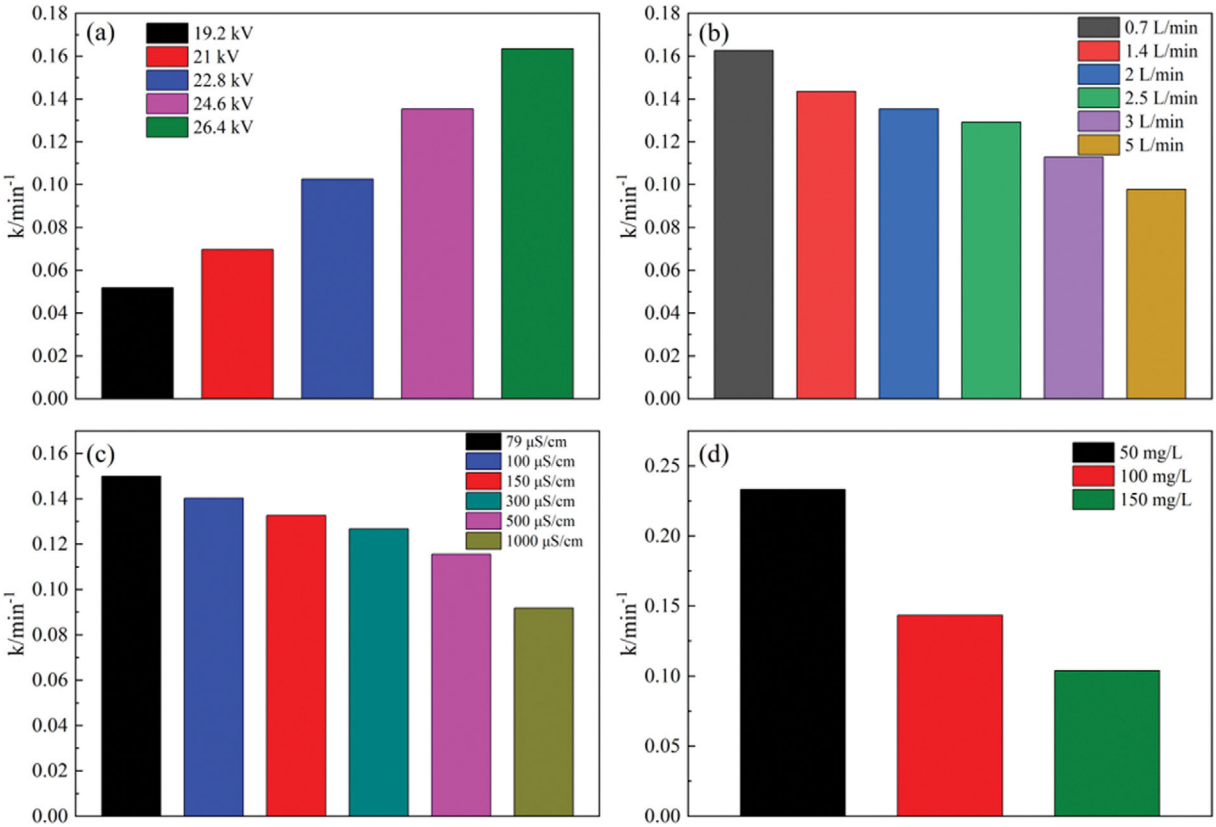

Fig. S4. Effect of various factors on the kinetic constants of OG degradation: (a) pulse peak voltage; (b) air flow rate; (c) initial conductivity of OG solution; (d) initial OG concentration.

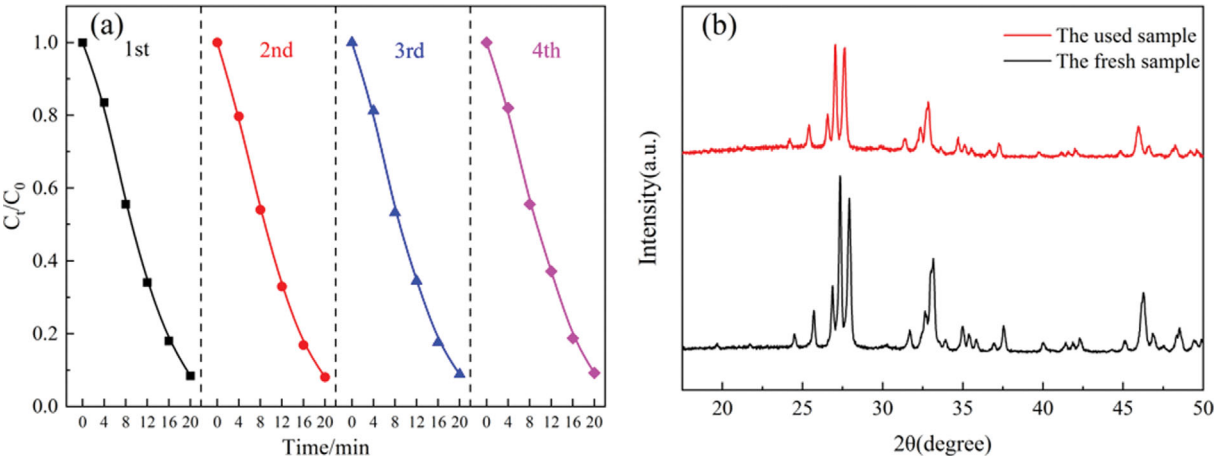

Fig. S5. (a) Cycling test of CB-8; (b) XRD patterns of CB-8 before and after use.

Fig. S3(c) exhibits the fine scanning spectrum of Fe 2p. The binding energies at 710.44 eV and 723.54 eV were attributed to the Fe $2p_{3/2}$ and Fe $2p_{1/2}$ respectively [3]. The separation distance between Fe $2p_{3/2}$ and Fe $2p_{1/2}$ was about 13.1 eV, confirming that the valence state of Fe presented as Fe^{3+}. Fig. S3(d) displays that the two peaks at 345.87 eV and 349.37 eV of Ca 2p corresponded to Ca $2p_{3/2}$ and Ca $2p_{1/2}$ spins of Ca^{2+}, respectively [4]. Therefore, the binding energies of four elements in the composites were consistent with those of Bi^{3+}, O^{2-}, Fe^{3+} and Ca^{2+} respectively, suggesting the successful preparation of the composites.

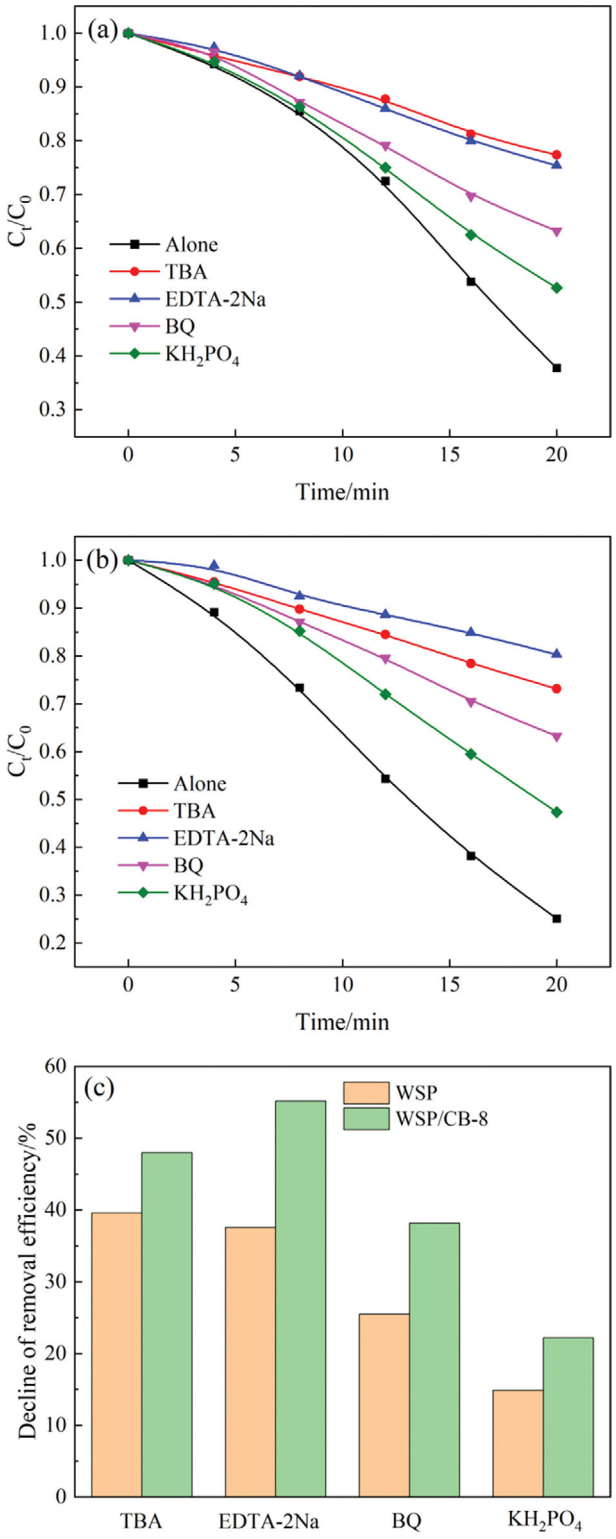

Fig. S6. Effect of scavengers in different systems: (a) WSP; (b) WSP/CB-8; (c) comparison of decline in removal efficiency.

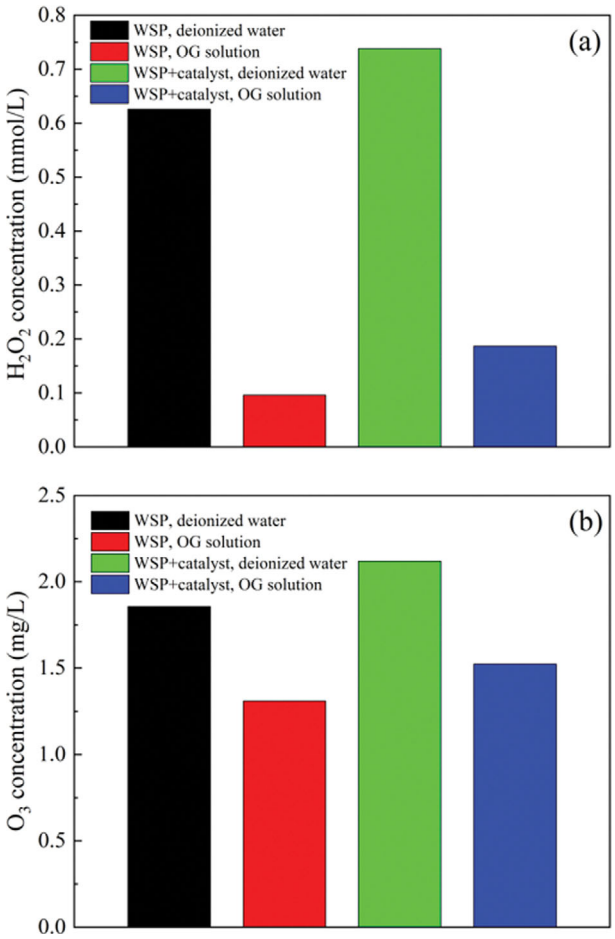

Fig. S7. Formation of (a) H_2O_2 and (b) O_3 in the two reaction systems.

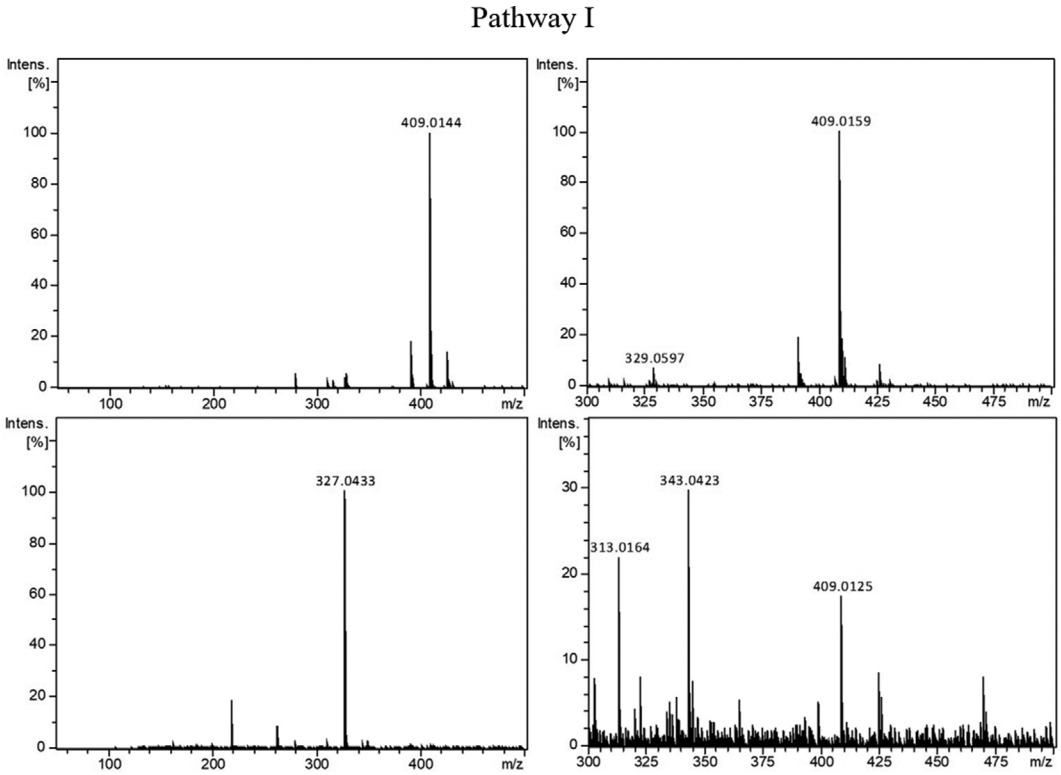

Fig. S8. LC-MS spectra of OG degradation in the WSP/CB-8 system.

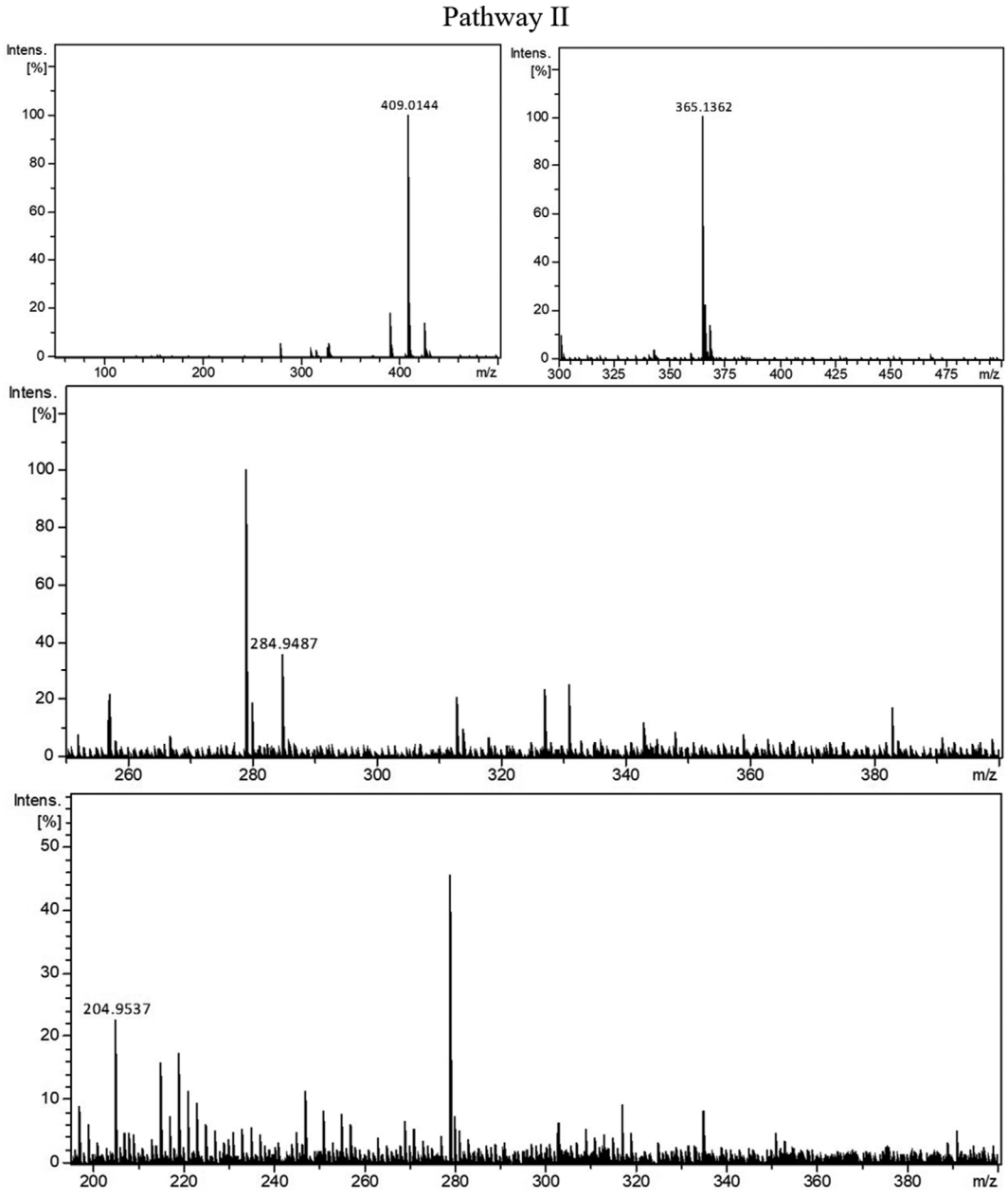

Fig. S8. Continued.

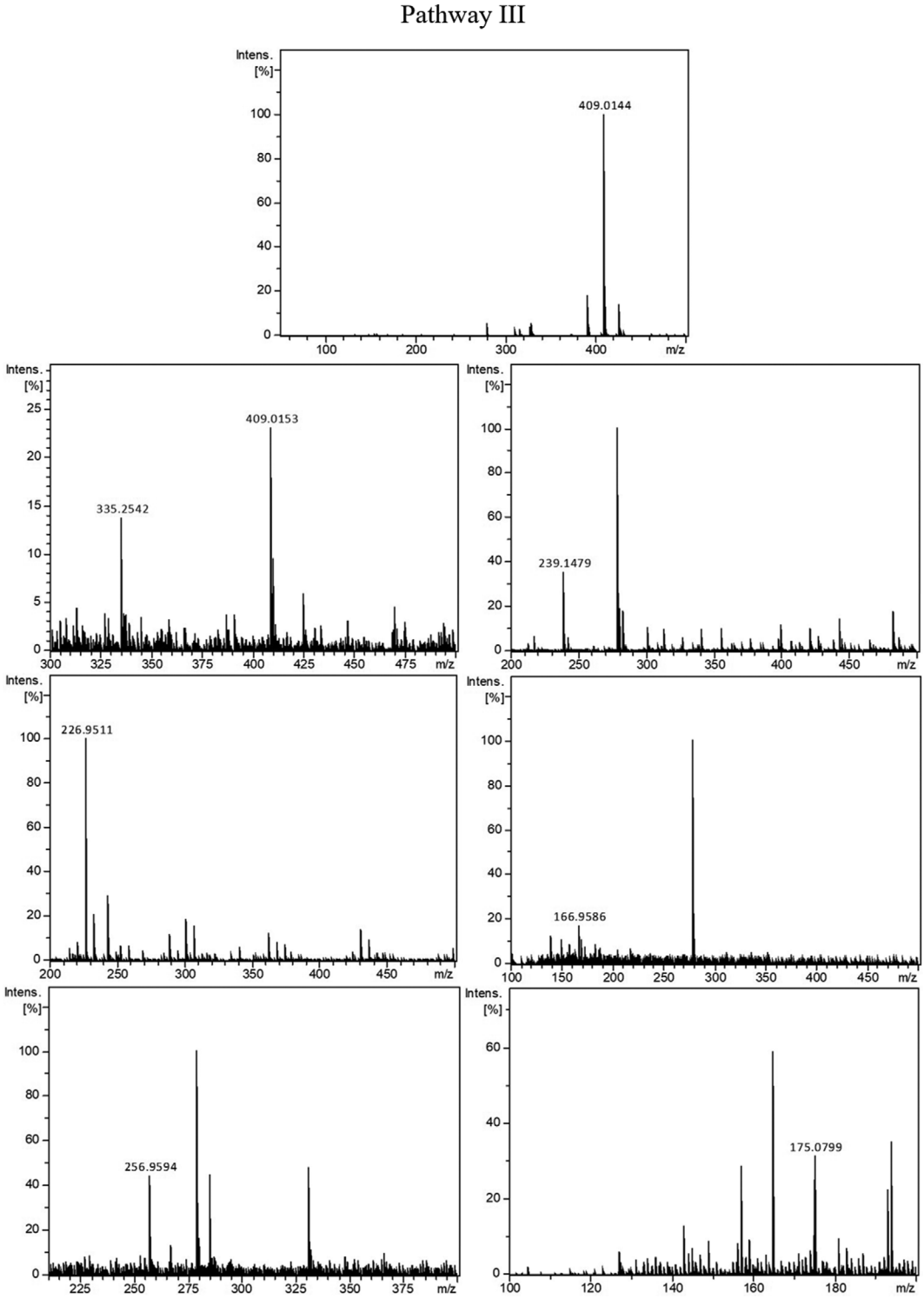

Fig. S8. Continued.

Table S1. The possible intermediates of the OG degradation in WSP/CB-8 system

Name code	Molecular formula	m/z	Chemical structure
OG	$C_{16}H_{12}N_2O_7S_2$	409	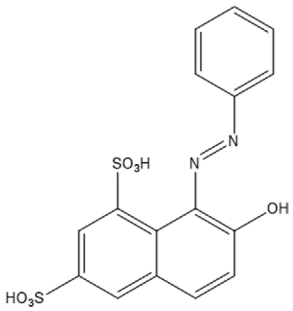
P1	$C_{16}H_{12}N_2O_4S$	329	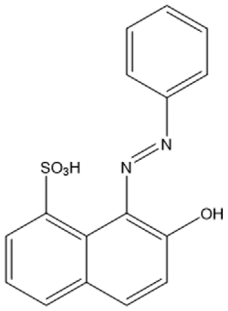
P2	$C_{16}H_{10}N_2O_4S$	327	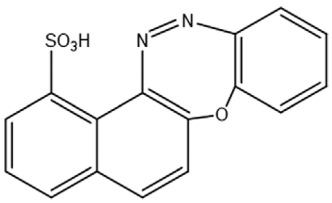
P3	$C_{16}H_{12}N_2O_3S$	313	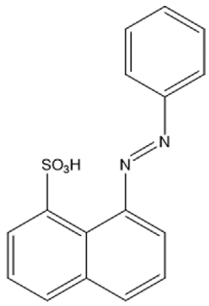
P4	$C_{16}H_{10}N_2O_5S$	343	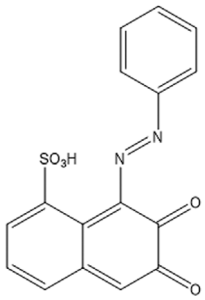
P5	$C_{10}H_8N_2O_9S_2$	365	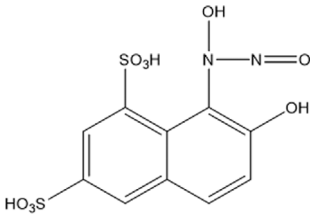

Table S1. Continued

Name code	Molecular formula	m/z	Chemical structure
P6	$C_{10}H_8N_2O_6S$	285	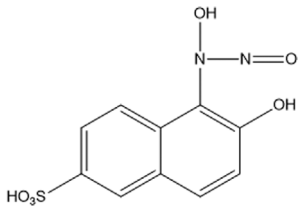
P7	$C_{10}H_8N_2O_3$	205	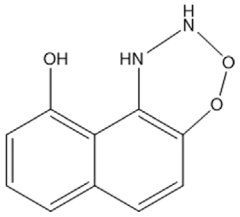
P8	$C_{10}H_9NO_8S_2$	335	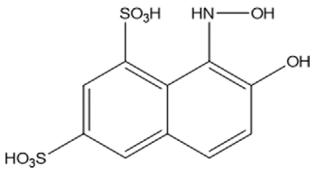
P9	$C_{10}H_9NO_4S$	239	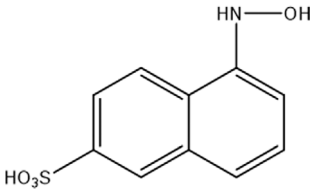
P10	$C_{10}H_{11}NO_5$	227	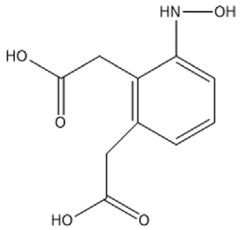
P11	$C_8H_6O_4$	167	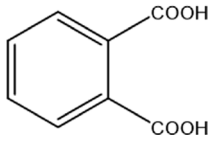
P12	$C_{10}H_9NO_5S$	257	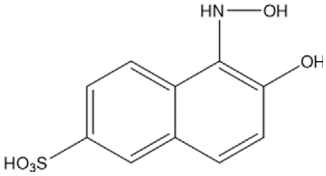
P13	$C_{10}H_9NO_2$	175	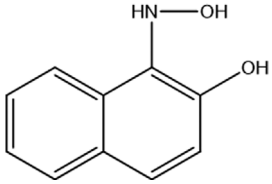

REFERENCES

1. W. Y. Gou, P. Wu, D. M. Jiang and X. M. Ma, *J. Alloys Compd.*, **646**, 437 (2015).
2. F. Liu, S. C. Dong, Z. X. Zhang, X. Q. Li, X. D. Dai, Y. P. Xin, X. W. Wang, K. Liu, Z. H. Yuan and Z. Zheng, *RSC Adv.*, **9**, 25750 (2019).
3. T. Yamashita and P. Hayes, *Appl. Surf. Sci.*, **254**, 2441 (2008).
4. N. K. Veldurthi, N. K. Eswar, S. A. Singh and G. Madras, *Int. J. Hydrogen Energy*, **43**, 22929 (2018).